A numerical analysis of the shear behavior of granular soil with fines

Beibing Dai [a,*], Jun Yang [b], Xiaodong Luo [b]

[a] Research Centre of Geotechnical Engineering and Information Technology, Sun Yat-sen University, Guangzhou 510275, China
[b] Department of Civil Engineering, The University of Hong Kong, Hong Kong, China

ABSTRACT

Shear behavior of granular soil with fines is investigated using the discrete element method (DEM) and particle arrangements and inter-particle contacts during shear are examined. The DEM simulation reveals that fine particles play a vital role in the overall response of granular soil to shearing. The occurrence of liquefaction and temporary reduction of strength is ascribed mainly to the loss of support from the fine particle contacts (S–S) and fine particle-to-large particle contacts (S–L) as a consequence of the removal of fine particles from the load-carrying skeleton. The dilative strain-hardening response following the strain-softening response is associated with the migration of fine particles back into the load-carrying skeleton, which is thought to enhance the stiffness of the soil skeleton. During shear, the unit normal vector of the large particle-to-large particle (L–L) contact has the strongest fabric anisotropy, and the S–S contact unit normal vector possesses the weakest anisotropy, suggesting that the large particles play a dominant role in carrying the shear load. It is also found that, during shear, fine particles are prone to rolling at contacts while the large particles are prone to sliding, mainly at the S–L and L–L contacts.

© 2015 Chinese Society of Particuology and Institute of Process Engineering, Chinese Academy of Sciences. Published by Elsevier B.V. All rights reserved.

Introduction

Over the past several decades, many laboratory investigations have been carried out in terms of the shear behavior of clean sands, and the behavior has been successfully described in the framework of critical state soil mechanics (CSSM). However, observations from the failures of soil structures involving sands (Ishihara, 1993; Seed & Harder, 1990) indicate that most in situ sands generally comprise a certain quantity of fine particles <0.074 mm in diameter. These are referred to as silty sands in geotechnical engineering practice and the mechanical behavior of silty sands, because of the presence of the fine particles, is complex and not yet fully understood.

A review of published laboratory studies on silty sands (Chu & Leong, 2002; Georgiannou, Burland, & Hight, 1990; Kuerbis, Negussey, & Vaid, 1988; Murthy, Loukidis, Carraro, Prezzi, & Salgado, 2007; Ni, Tan, Dasari, & Hight, 2004; Pitman, Robertson, & Sego, 1994; Thevanayagam & Mohan, 2000; Yamamuro & Lade, 1997; Yang & Wei, 2012; Zlatović & Ishihara, 1997) indicates that the CSSM theory does not adequately describe the behavior of silty sands. For example, it was reported by Yamamuro and Lade (1997)

that silty sand specimens with the same fines content, sheared at different consolidation pressures, tended to demonstrate a "reverse behavior" in that an increase in the consolidation pressure gave rise to an increase in dilation and enhanced the ability of the specimen to resist liquefaction. This is contrary to the normal behavior of clean sands predicted by the CSSM theory. The study of Thevanayagam and Mohan (2000) also showed that two silty sands, having the same initial global void ratio and fines content, behaved in a manner that could not be described in the framework of CSSM: the specimen at a higher confining pressure exhibited higher shear strength at a steady state.

The state parameter ψ, defined as the difference between the current global void ratio and the critical void ratio at the same mean effective stress (Been & Jefferies, 1985), is a useful parameter in describing sand behavior in the framework of CSSM (Li & Dafalias, 2000; Wood, Belkheir, & Liu, 1994; Yang & Li, 2004; Yang, 2002). The state parameter, however, does not work effectively for silty sand. As shown in Fig. 1(a), Foundry sand with a specific fines content of 12% shows a trend of decreasing contractiveness with increasing ψ (Thevanayagam & Mohan, 2000), a reverse trend compared with clean sand (Fig. 1(b)). In particular, many published studies have found that no unique critical state line can be determined in the e–log p' plane for silty sand (Been & Jefferies, 1985; Murthy et al., 2007).

* Corresponding author. Tel.: +86 2084111124.
  E-mail addresses: beibing_dai@yahoo.com (B. Dai), junyang@hku.hk (J. Yang).
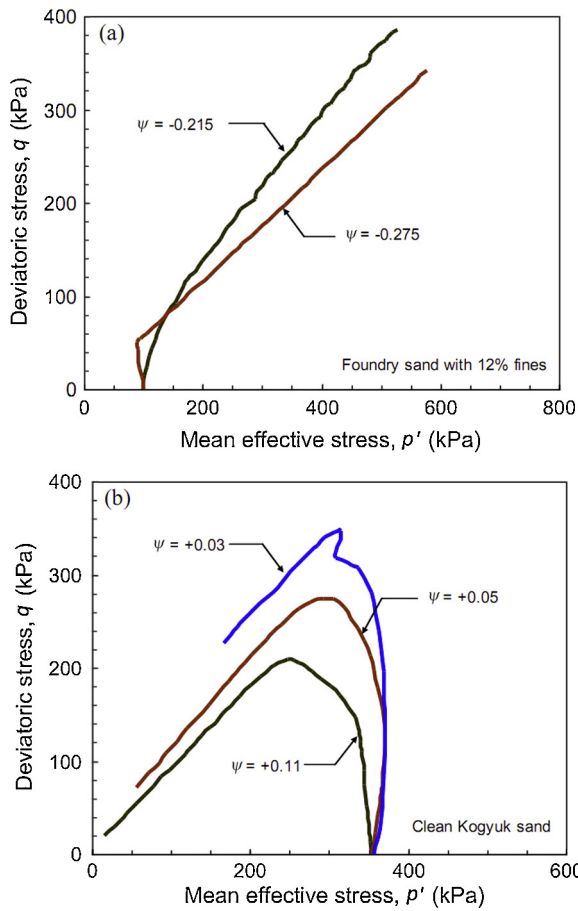
Fig. 1. Influence of state parameter on the shear behavior of granular soil: (a) foundry sand with fines (Thevanayagam & Mohan, 2000) and (b) clean Kogyuk sand (Been & Jefferies, 1985).

Fig. 2. Particle shape and size distributions considered in this study. Grading curve A has 10% particles <0.26 mm and $fc \sim 2\%$, grading curve B has 5% particles <0.26 mm and $fc \sim 1\%$, and grading curve C represents clean sand with grains in the 0.26–0.66 mm size range.

Some researchers have ascribed the incompatibility of the framework of CSSM with silty sand to the use of the global void ratio or ψ (Bobei, Lo, Wanatowski, Gnanendran, & Rahman, 2009; Georgiannou et al., 1990; Lade & Yamamuro, 1997; Mitchell, 1976; Ni et al., 2004; Rahman, Lo, & Gnanendran, 2008; Thevanayagam & Mohan, 2000). These authors considered that the fine particles were easily trapped in the voids formed between large particles and hence made little contribution to the force chains. In this respect, an alternative state variable, known as the skeleton void ratio, e_s, was proposed for silty sand by treating all of the fine particles as void spaces (e.g. Georgiannou et al., 1990; Mitchell, 1976). This index was then modified as an equivalent skeleton void ratio e_{se} by introducing a parameter, b, that considers partial participation of fine particles in the force chains (e.g. Ni, Tan, Dasari, & Hight, 2004; Thevanayagam, Shenthan, Mohan, & Liang, 2002):

$$e_{se} = \frac{e + (1-b)fc}{1-(1-b)fc}, \qquad (1)$$

where e is the global void ratio, fc is the fines content, and b denotes the portion of fine particles present in the force chains. Several issues were clarified by the use of the equivalent skeleton void ratio. First, a unique critical state line could be determined in the e_{se}–log p' plane by the best-fit approach using a back-calculated b value (Rahman et al., 2008; Thevanayagam, Shenthan, Mohan, & Liang, 2002; Yang, Sandven, & Grande, 2006). Notably, however, the factor b was treated in these studies as a constant throughout the loading process, which does not reflect its originally defined physical meaning (Dai, 2010).
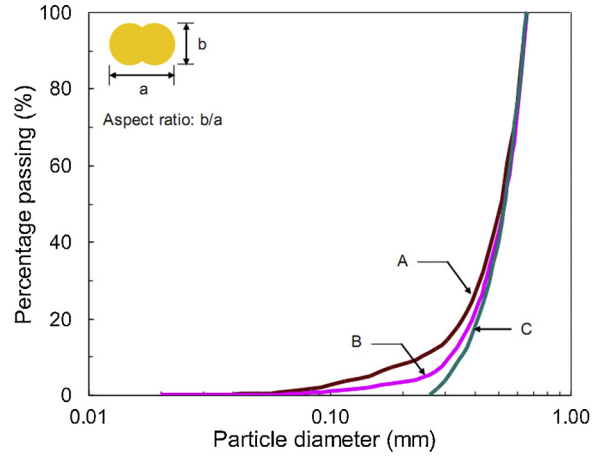
The complexity in the behavior of silty sand arises from its particulate nature, and particularly the presence of the fine particles. To develop a fundamental understanding of the shear properties of silty sand, it is necessary to examine the spatial arrangements of the fine particles in the soil skeleton and their interactions with coarse particles during the loading process. This is the motivation of this work and, by means of grain-scale modeling using the discrete element method (DEM) (Cundall, 1971), a series of numerical simulations have been performed and the results are presented and interpreted.

DEM model and data interpretation

Numerical model implementation

The program PFC2D (Itasca, 2005) was used to conduct biaxial test simulations in undrained conditions. Numerical specimens were composed of idealized particles, each of which had two circular constituent particles clumped together (Fig. 2) to take into account the non-circular shape of soil particles. Each clumped particle was assumed to behave as a rigid body with an aspect ratio of 0.6, and the two constituent particles were not allowed to break apart during loading. The size of a clumped particle was described by an equivalent particle diameter – the diameter of a circular particle with the same cross sectional area as the clumped particle. The linear elastic contact model was used to describe the contact behavior between particles, and the friction behavior at contacts was assumed to observe the Coulomb friction law. Both the normal and tangential stiffnesses of the contact were assumed to be 1.0×10^9 N/m, and a friction coefficient of 0.5 was adopted.

Three grading curves were considered in this study (Fig. 2). Grading curve C serves as the reference curve, representing clean sand with particles in the size range of 0.26–0.66 mm. To study the effect of fines, different amounts of finer particles were added to form two different materials, as represented in grading curves A and B. Grading curve A represents a silty sand with 10% particles <0.26 mm and $fc \sim 2\%$. Grading curve B represents a silty sand with 5% particles <0.26 mm and $fc \sim 1\%$.

All numerical specimens were prepared using the gravitational deposition method. As illustrated in Fig. 3(a), particles with random orientations were initially generated in a designated domain, and the gravity field was then introduced with the gravitational forces applied to all particles in a vertical direction. In doing so,
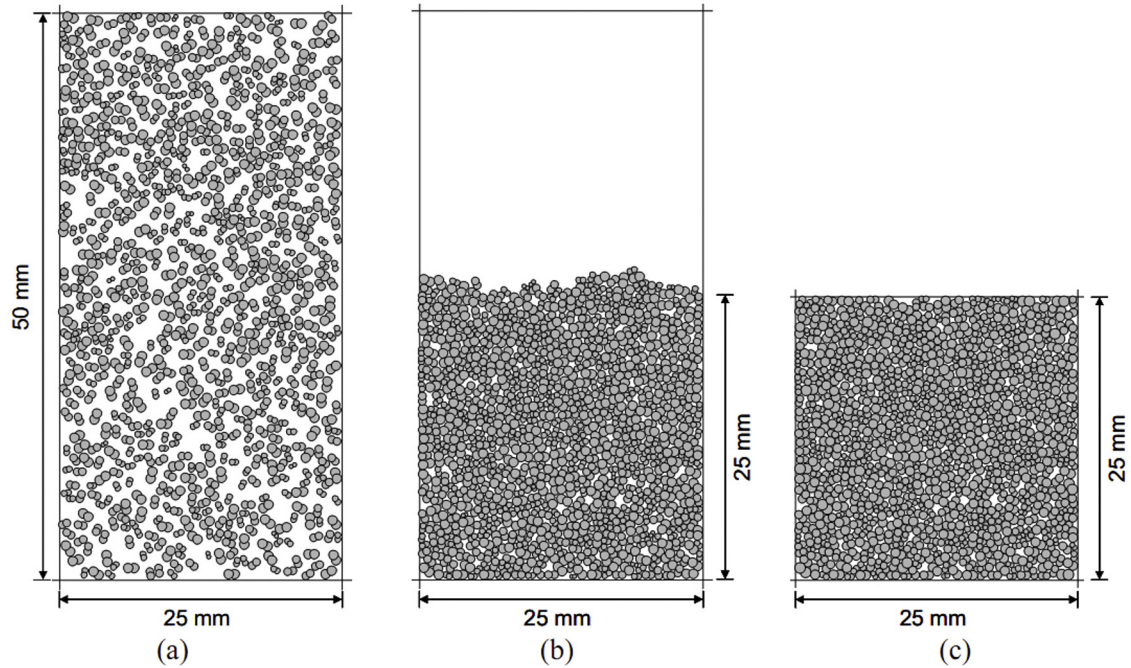
Fig. 3. Sample preparation by gravitational deposition: (a) initial particle distribution, (b) deposition completed, and (c) final specimen.

Table 1
Sample information.

Test name	Grading curve	Global void ratio, e	Particle number, N	Confining pressure, p (kPa)
T-1	A	0.2157	9013	1000
T-2	B	0.2175	5212	1000
T-3	C	0.2171	2881	1000

particles descended and were deposited on the bottom boundary, as shown in Fig. 3(b). At the end of deposition, a 25 mm × 25 mm area (Fig. 3(c)) was chosen as the final specimen, and compaction was then performed via simultaneous contraction of the four rigid boundary walls. All numerical specimens were consolidated to a confining pressure of 1000 kPa, with a global void ratio of ~0.217. Undrained shearing was achieved by moving the two loading walls whilst maintaining a constant sample volume. Tables 1 and 2 present parameters of the contact model and sample information.

It must be noted that a 3D DEM model requires a higher computational cost and is more time-consuming than a 2D model given that both fine and large particles need to be generated to reproduce the fines and the coarse soil grains, respectively. Additionally, many DEM simulations on soil behavior in the literature have demonstrated that 2D simulations are able to reproduce the main features of soil behavior (Gu, Yang, & Huang, 2013; Khalili & Mahboubi, 2014; Mahmud Sazzad, 2014; Yang & Dai, 2011). Therefore, 2D simulations were chosen for this study although further work involving 3D DEM simulations will also be pursued and reported in future.

Table 2
Model parameters.

Particle density, ρ (g/cm^3)	2.65
Aspect ratio, R_a	0.6
Inter-particle friction, μ_s	0.5
Wall friction, μ_w	0.0
Normal and tangential stiffness, k_n and k_s (N/m)	10^9
Wall stiffness, k_w (N/m)	10^9
Damping factor, α	0.7

Macro- and micro-indices

For biaxial tests, the mean effective stress (p') and deviatoric stress (q) can be defined as: $p' = (\sigma_1 + \sigma_2)/2$ and $q = \sigma_1 - \sigma_2$, respectively, where σ_1 and σ_2 are the major and minor principal stresses. The axial strain (ε_a) is estimated from boundary movements, where $\varepsilon_a = \Delta L/L$; L is the original length of the confining wall, and ΔL is the shortened length resulting from movement of the loading walls.
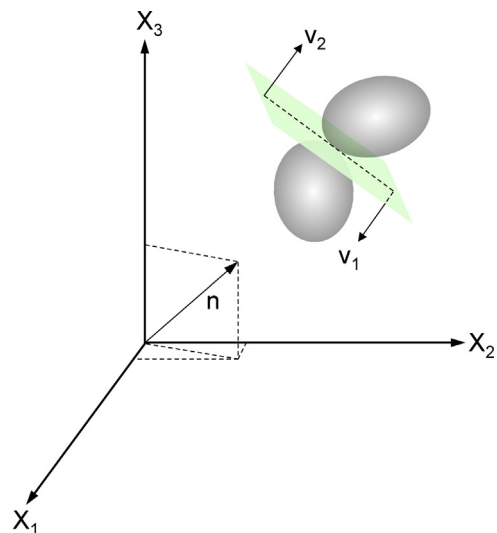

Fig. 4. Geometrical description of vectors: $\mathbf{v}_1$ and $\mathbf{v}_2$ = contact unit normal vectors and $\mathbf{n}$ = unit vector in a Cartesian coordinate system.
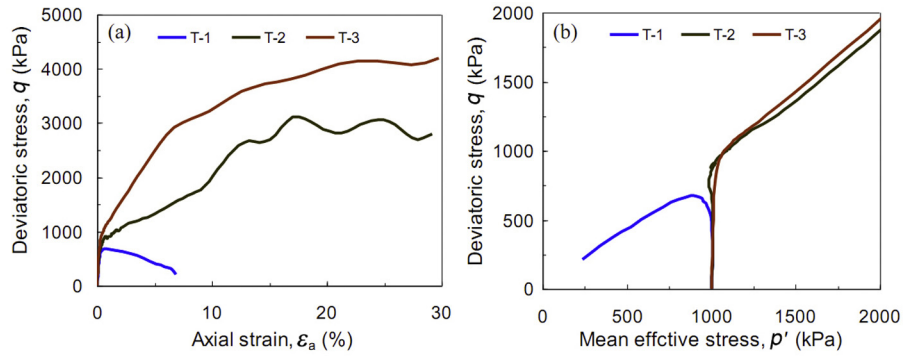
Fig. 5. Macroscopic shear behavior of three specimens, T-1, T-2, and T-3, determined by numerical simulation: (a) q vs ε_a and (b) q vs p'. Note that specimen T-1, with the highest fines content, behaves in the most contractive manner and liquefies upon shearing, whereas T-3 (clean sand) exhibits the most dilative behavior, achieving the highest deviatoric stress and mean effective stress at the large strain.
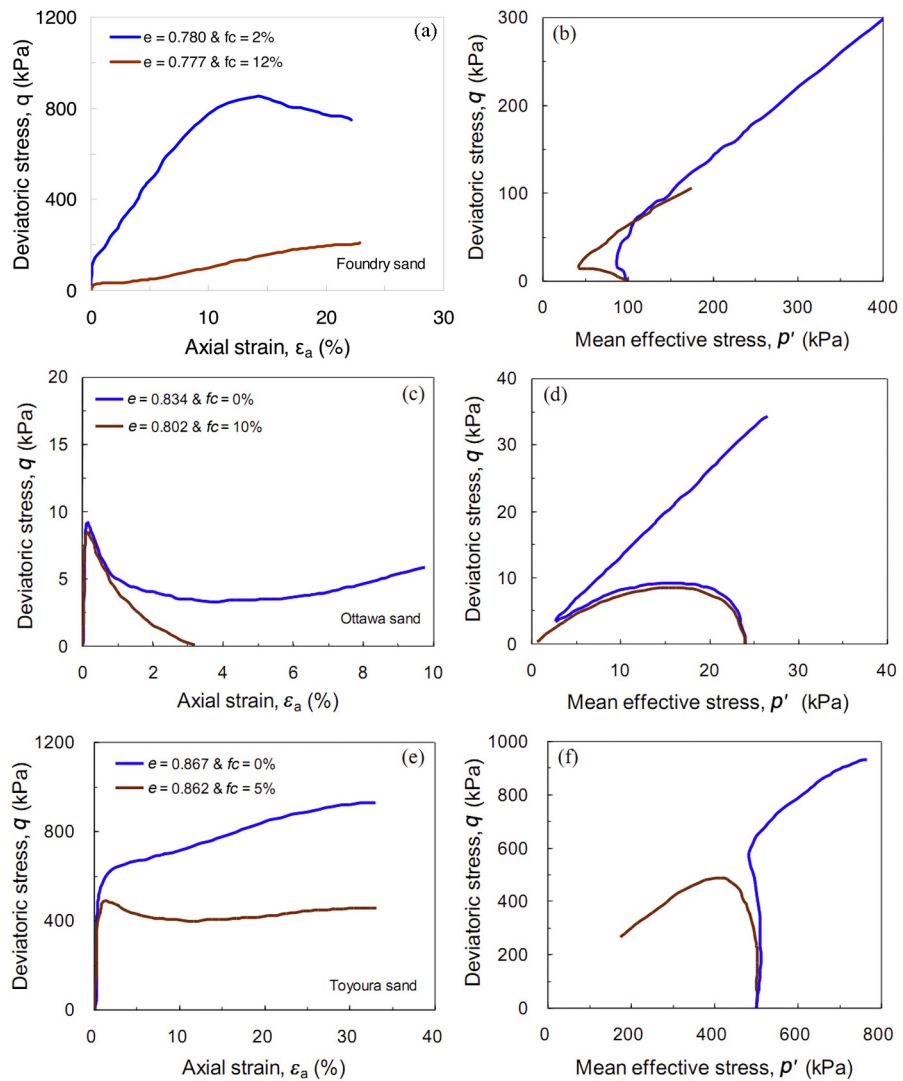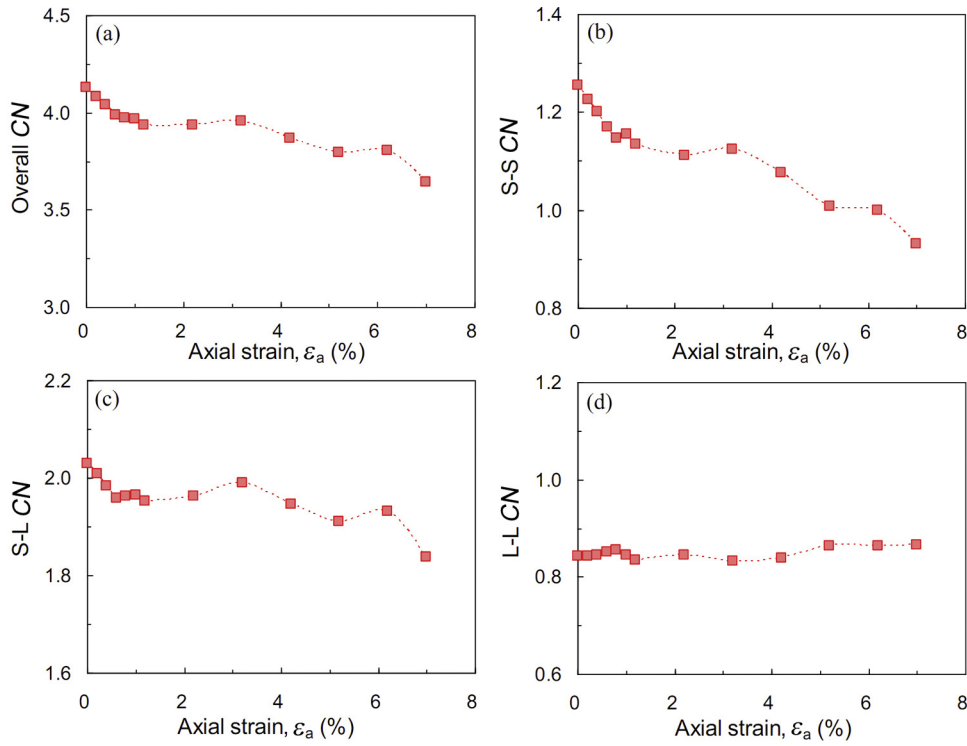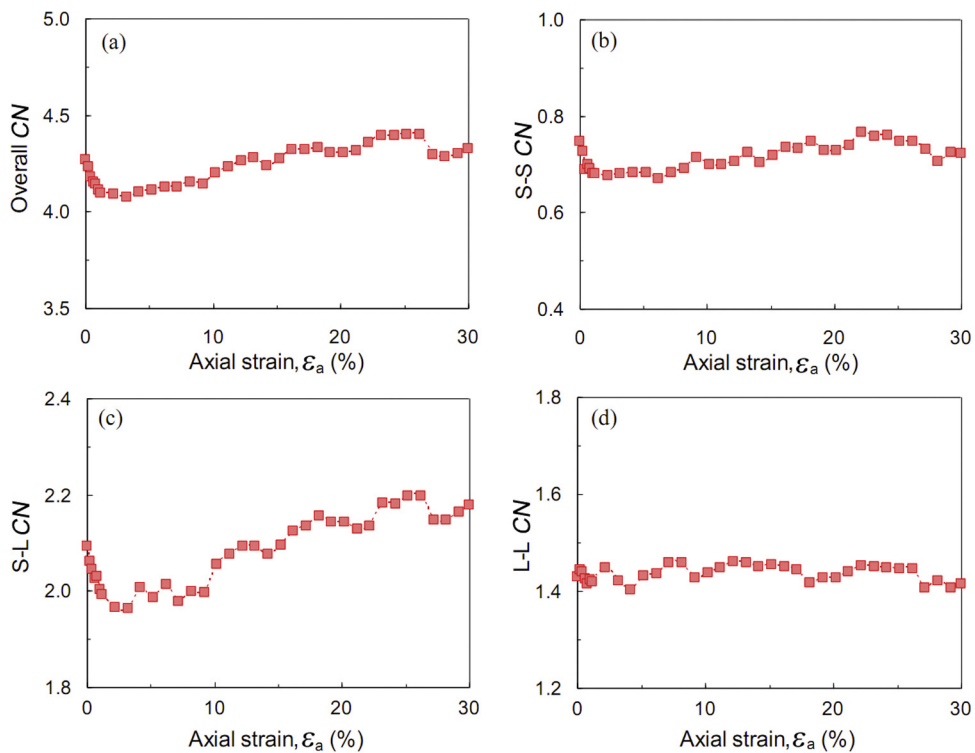

Fig. 6. Previous laboratory test findings of shear behavior: (a and b) Thevanayagam and Mohan (2000), (c and d) Lade and Yamamuro (1997), and (e and f) Yang and Wei (2012).

Fig. 7. Evolution of coordination numbers (*CN*) for specimen T-1 according to grain type contacts: (a) overall *CN*, (b) S–S *CN*, (c) S–L *CN*, and (d) L–L *CN*.

Fig. 8. Evolution of coordination numbers (*CN*) for specimen T-2 according to grain type contacts: (a) overall *CN*, (b) S–S *CN*, (c) S–L *CN*, and (d) L–L *CN*.

Fig. 9. Relationships between the particle number and the contact number at different shear strain levels for specimen T-1: (a) N_L vs N_C and (b) N_S vs N_C.

To quantify the microstructures of the granular assembly, the contact unit normal vector, as depicted in Fig. 4, was used to formulate the fabric tensor. The second-rank fabric tensor (Oda, 1982, 1999) is expressed as:

$$\mathbf{F}_{ij} = \frac{1}{2N} \sum_{k=1}^{2N} \mathbf{n}_i^k \mathbf{n}_j^k, \tag{2}$$

where N is the contact number and $\mathbf{n}_i^k$ ($i = 1$–3) are the direction cosines of the contact unit normal vector $\mathbf{n}^k$ with reference to the axes X_i ($i = 1$–3) in a Cartesian coordinate system (Fig. 4). By introducing a density function $E(n)$, the second-rank fabric tensor $\mathbf{F}_{ij}$ can be rewritten into the integral form (Rothenburg & Bathurst, 1989):

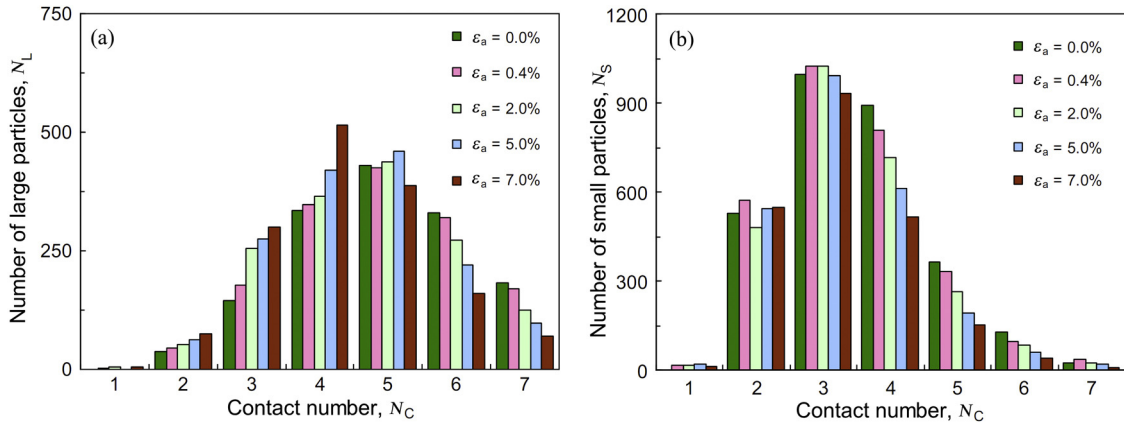$$\mathbf{F}_{ij} = \int_{\Omega} E(n)\mathbf{n}_i\mathbf{n}_j d\Omega, \tag{3}$$
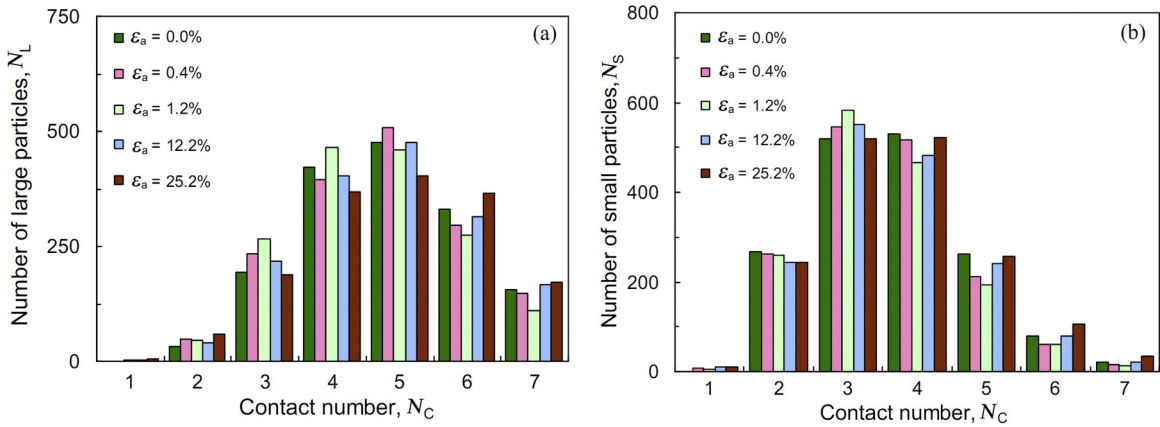

Fig. 10. Relationships between the particle number and the contact number at different shear strain levels for specimen T-2: (a) N_L vs N_C and (b) N_S vs N_C.
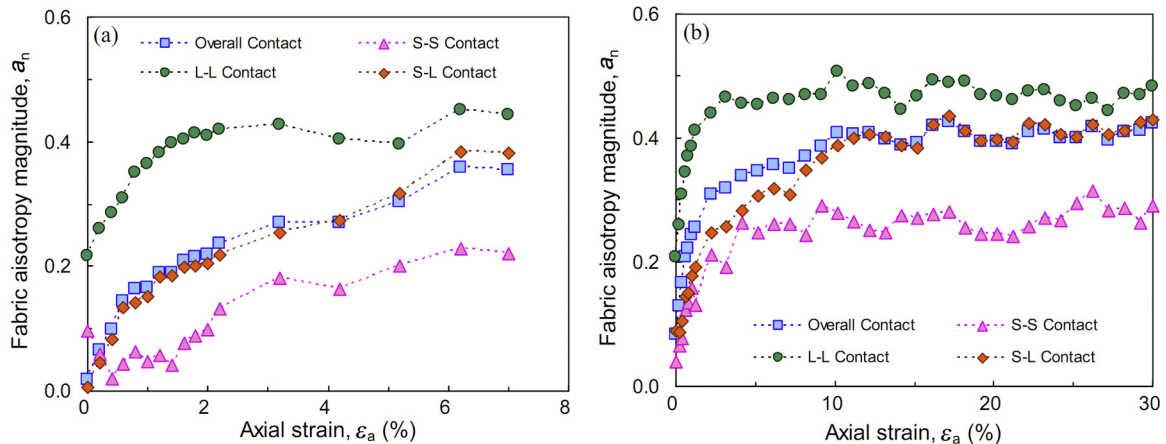

Fig. 11. Evolution of the magnitudes of fabric anisotropy of contact unit normal vectors for specimens: (a) T-1 and (b) T-2.

where Ω is the representative elemental volume and the expression of $E(n)$ is given as:

$$E(n) = E_0(1 + d_{ij}n_i n_j), \tag{4}$$

or

$$E(\phi) = E_0\{1 + a_n \cos 2(\phi - \phi_n)\}, \tag{5}$$

where E_0 denotes the distribution probability density at an isotropic state, d_{ij} is a second-rank tensor describing the deviations from the isotropic distribution, ϕ refers to a direction angle of interest, a_n is the magnitude of anisotropy, and ϕ_n indicates the principal direction of anisotropy. The value of $E(\phi)$ in Eq. (5) represents the distribution probability of contact unit normal vectors in the direction denoted by the angle ϕ. It is evident that the parameters a_n and ϕ_n are two important indices that characterize the fabric anisotropy, and these can be determined by equating Eq. (2) to Eq. (3) as follows:

$$a_n = \sqrt{d_{11}^2 + d_{12}^2}, \quad \text{and} \quad \phi_n = \frac{1}{2}\arctan\left(\frac{d_{12}}{d_{11}}\right). \tag{6}$$

Coordination number is an effective index to characterize the packing state of a granular assembly at a microscopic level and is defined as the average contact number per particle. It must be noted that there are inevitably some particles without contacts or with only one contact and these do not contribute to the force chains in the soil skeleton. Therefore, an alternative coordination number,

known as the mechanical coordination number (Thornton, 2000), was used to better characterize the packing state, and is defined as follows:

$$CN = \frac{2C - N_1}{N - N_1 - N_0}, \tag{7}$$

where C is the contact number, N is the particle number, N_1 is the number of particles with only one contact and N_0 is the number of particles without contacts.

Simulation results and discussion

Macroscopic observations

Macroscopic shear behavior of the three specimens is presented in Fig. 5. Specimen T-1 (grading curve A in Fig. 2), with the highest content of fine particles, behaved in the most contractive manner, liquefying at the end of shearing. Specimen T-3 (grading curve C in Fig. 2), representing clean sand without fines, exhibited the most dilative behavior, achieving the highest deviatoric stress and mean effective stress at large strain. The response of specimen T-2 (grading curve B in Fig. 2) appears to be intermediate, manifested by the occurrence of the phase transformation state (Yang & Dai, 2011). The deviatoric stress of specimen T-2 is well below that of specimen T-3, but its overall behavior is more dilative than specimen

(a) $\varepsilon_a = 0.0\%$, $a_n = 0.039$, $\phi_n = 156.0°$

(b) $\varepsilon_a = 1.2\%$, $a_n = 0.132$, $\phi_n = 101.2°$

(c) $\varepsilon_a = 12.2\%$, $a_n = 0.252$, $\phi_n = 92.50°$

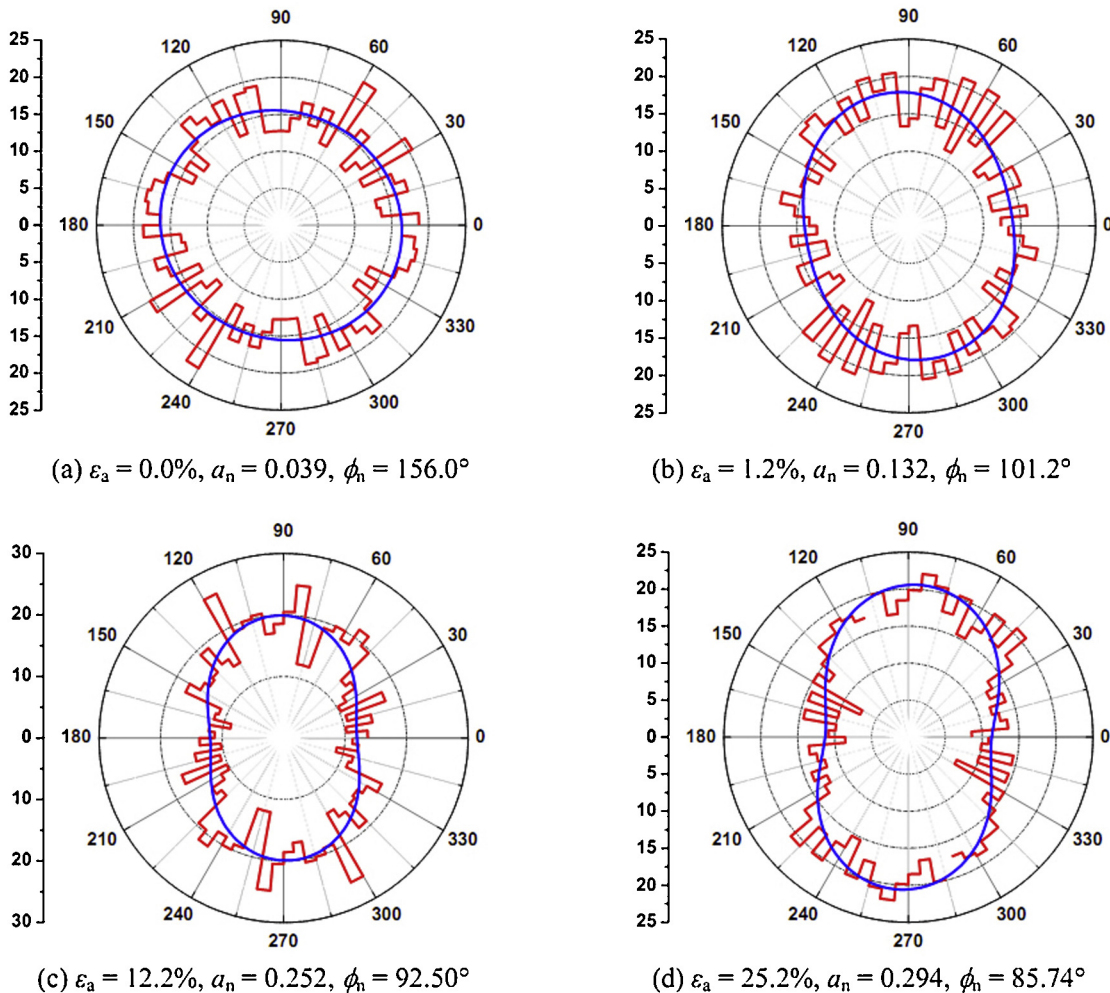(d) $\varepsilon_a = 25.2\%$, $a_n = 0.294$, $\phi_n = 85.74°$

Fig. 12. Angular distribution probability density (%) of the S–S contact unit normal vector for specimen T-2.

T-1. Similar observations can be made from the stress paths in the q–p' plane (Fig. 5(b)).

It is worth noting that the shear responses shown in Fig. 5 are consistent with the findings of Yamamuro and Lade (1997), Thevanayagam and Mohan (2000), and Yang and Wei (2012), as reproduced in Fig. 6. These test results indicated that the participation of fine particles in the soil skeleton led to an increase of contractiveness and liquefaction potential.

Microscopic observations

Coordination number

The mechanical coordination number calculated for the whole granular assembly is referred to herein as the overall coordination number (overall CN). It is decomposed into three parts in this study: (1) S–S coordination number (S–S CN)–the coordination number contributed by the contacts between fine particles; (2) S–L coordination number (S–L CN)–the coordination number contributed by the contacts between fine and large particles; and (3) L–L coordination number (L–L CN)–the coordination number contributed by the contacts between large particles.

The evolution of the four coordination numbers defined above for specimens T-1 and T-2 is presented in Figs. 7 and 8, respectively. The overall CN for specimen T-1, which underwent complete liquefaction, shows a monotonic decrease with axial strain. It is found

that the decreases of both the S–S CN and S–L CN account mainly for the decrease of the overall CN, since the variation of the L–L CN is not significant. The important implication is that the occurrence of liquefaction in specimen T-1 is closely linked with the movement of fine particles within the soil skeleton. It can be inferred that, upon shearing, a number of fine particles exit the force chains, and some large particles, due to the loss of the supporting effect from the fine particles, also exit, giving rise to the continuous loss of the S–S and S–L contacts and thus liquefaction occurs.

Specimen T-2 (non-liquefied) shows a temporary decrease in the S–S and S–L CN upon initial shearing; however, further shearing leads to a rebound of these two coordination numbers (Fig. 8). Such a trend is not observed in the L–L CN, which remains almost unchanged during shear. Evidently, the S–S CN and S–L CN dominate the variations in the overall CN, and thus fine particles clearly play a crucial role in the evolution of the overall CN and, consequently, in the overall response of specimen T-2 to shearing. The interim decreases of the S–L CN and S–S CN suggest that the removal of a number of fine particles from the soil skeleton has occurred. The particle rearrangements and microstructure reorganizations involved appear to render a relatively soft soil skeleton, leading to temporary contractiveness, as evidenced by the macro shear behavior shown in Fig. 5. The subsequent increases of both S–L CN and S–S CN indicate the re-entry of fine particles into the force chains, leading to a stiffer soil skeleton and more dilative behavior.

(a) $\varepsilon_a = 0.0\%$, $a_n = 0.088$, $\phi_n = 141.0°$

(b) $\varepsilon_a = 1.2\%$, $a_n = 0.192$, $\phi_n = 100.1°$

(c) $\varepsilon_a = 12.2\%$, $a_n = 0.406$, $\phi_n = 93.66°$

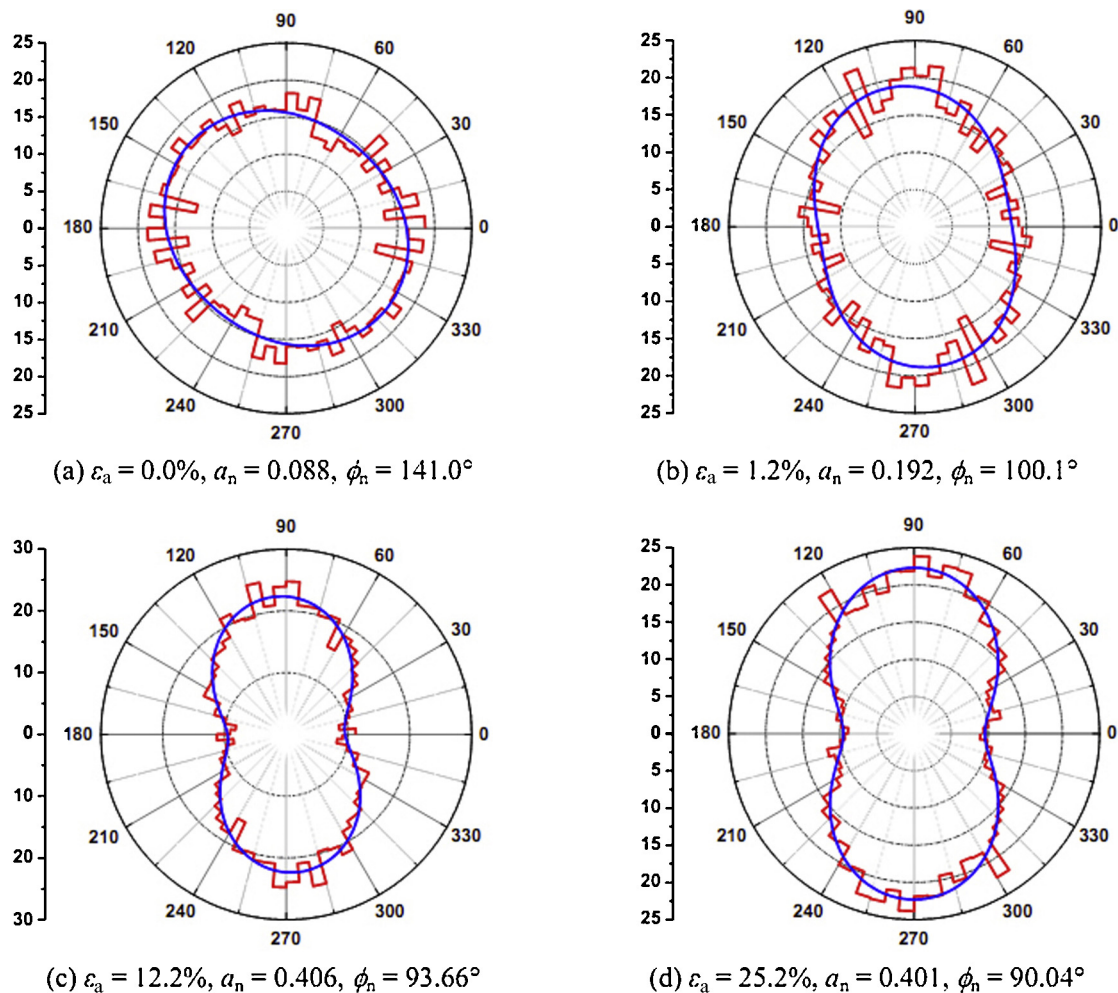(d) $\varepsilon_a = 25.2\%$, $a_n = 0.401$, $\phi_n = 90.04°$

Fig. 13. Angular distribution probability density (%) of the S–L contact unit normal vector for specimen T-2.

In Fig. 9(a) the statistics of the numbers of large particles corresponding to different contact numbers are shown for specimen T-1 at different shear strains (ε_a). Similar statistics for small particles are shown in Fig. 9(b). It is interesting to note that the number of large particles with more than five contacts decreases with increasing strain, whereas the number of large particles with less than five contacts increases with increasing strain. This suggests a continuous loss of contacts for large particles during shear, which is mainly induced by the disintegration of the S–L contacts. Conversely, the number of small particles with more than three contacts decreases with increasing strain. It appears that, for large particles, $N_C = 5$ can be used as an approximate criterion for judging whether such particles tend to lose or gain contacts, whereas $N_C = 3$ can be adopted for fine particles. The lower value for fine particles may be caused by the fact that these particles can be more easily confined in the voids so that their degree of participation in the soil skeleton is lower. Similarly, it can be observed in Fig. 10(a) for specimen T-2 that, the N_L with the contact number N_C above five decreases first upon initial shearing, but then increases at large shear strains. Conversely, a nearly reverse trend occurs when $N_C < 5$. In Fig. 10(b), the number of fine particles with a high contact number ($N_C > 3$) decreases first and then increases with further shearing, and exhibits the inverse tendency when $N_C < 3$. This indicates that fine particles in specimen T-2 first move out of the soil skeleton at the initial shearing stage, and subsequently migrate back into the soil skeleton upon further shearing.

Fabric anisotropy

This section presents an analysis of fabric anisotropy in terms of the contact unit normal vector. Similar to the differentiation of the coordination number, the contact unit normal vector is differentiated here into the S–S, S–L, and L–L contact unit normal vectors, and the overall contact unit normal vector is defined with respect to all the inter-particle contacts.

The evolution of the fabric anisotropy magnitude, a_n, of the four contact unit normal vectors is shown in Fig. 11. For specimen T-2, the anisotropy magnitudes of the S–S, S–L, and L–L contact unit normal vectors increase steadily at the initial shearing stage, and so does the a_n of the overall contact unit normal vector. This signifies that the accumulating S–S, S–L, and L–L contacts tend to be orientated in the loading direction such that they are able to effectively carry the external load. This finding is verified by observations of the rose diagrams describing the angular distribution of contact unit normal vectors. It is observed in Figs. 12–14 that a_n of the S–S, S–L, and L–L contact unit normal vectors where $\varepsilon_a = 1.2\%$ are distinctly larger than those in the initial state, and the principle directions of anisotropy (ϕ_n) are ~90°, i.e., orientated nearby the loading direction. Additionally, it is noted that from $\varepsilon_a = 0.0\%$ to $\varepsilon_a = 1.2\%$, ϕ_n undergoes a considerable rotation toward the loading direction for the S–S and S–L contact unit normal vectors.

Upon further shearing, the fabric anisotropy magnitudes reach an almost stable state at large shear strains. The rose diagrams in Figs. 12–14 also show that the angular distributions of contact
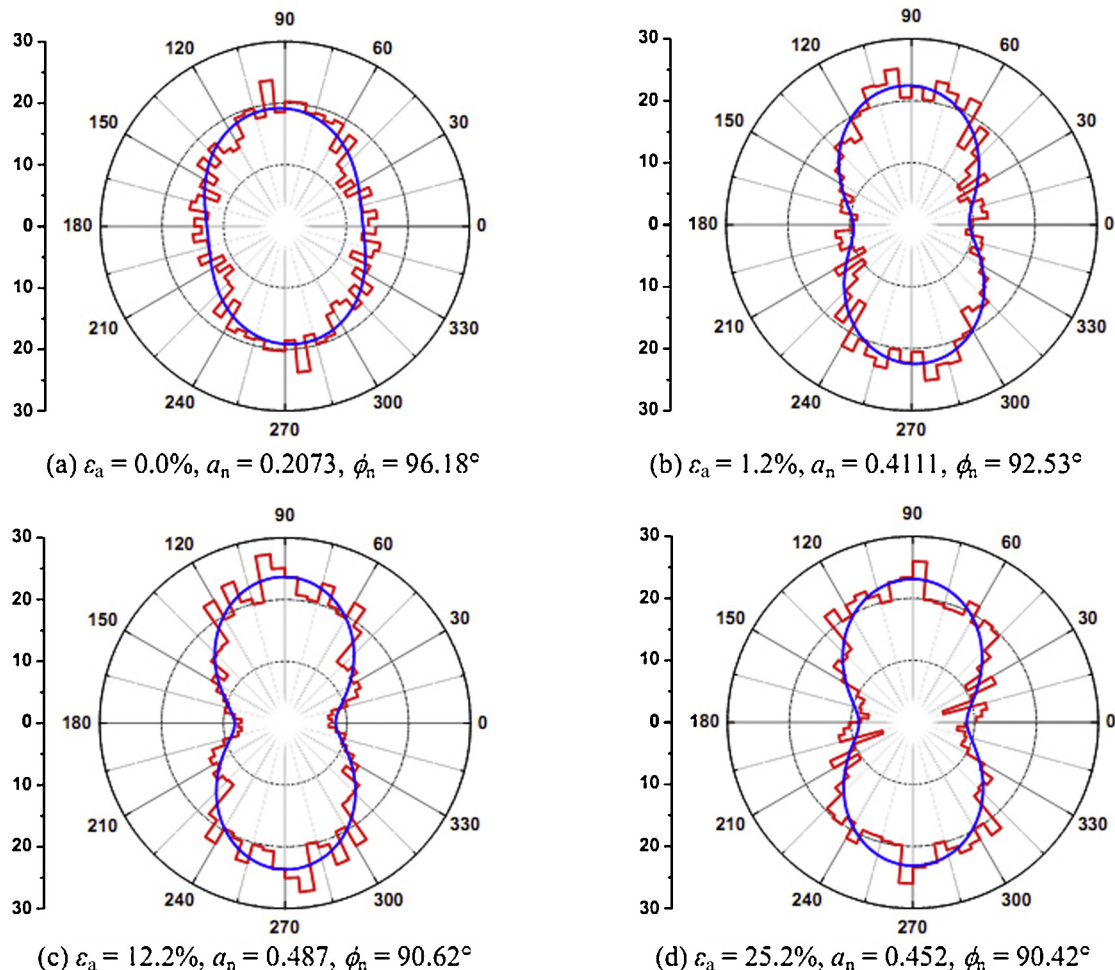

(a) $\varepsilon_a = 0.0\%$, $a_n = 0.2073$, $\dot{\phi}_n = 96.18°$

(b) $\varepsilon_a = 1.2\%$, $a_n = 0.4111$, $\phi_n = 92.53°$

(c) $\varepsilon_a = 12.2\%$, $a_n = 0.487$, $\dot{\phi}_n = 90.62°$

(d) $\varepsilon_a = 25.2\%$, $a_n = 0.452$, $\phi_n = 90.42°$

Fig. 14. Angular distribution probability density (%) of the L–L contact unit normal vector for specimen T-2.

(a) $\varepsilon_a = 0.0\%$, $a_n = 0.083$, $\phi_n = 114.5°$

(b) $\varepsilon_a = 1.2\%$, $a_n = 0.255$, $\phi_n = 95.99°$

(c) $\varepsilon_a = 12.2\%$, $a_n = 0.408$, $\phi_n = 92.30°$

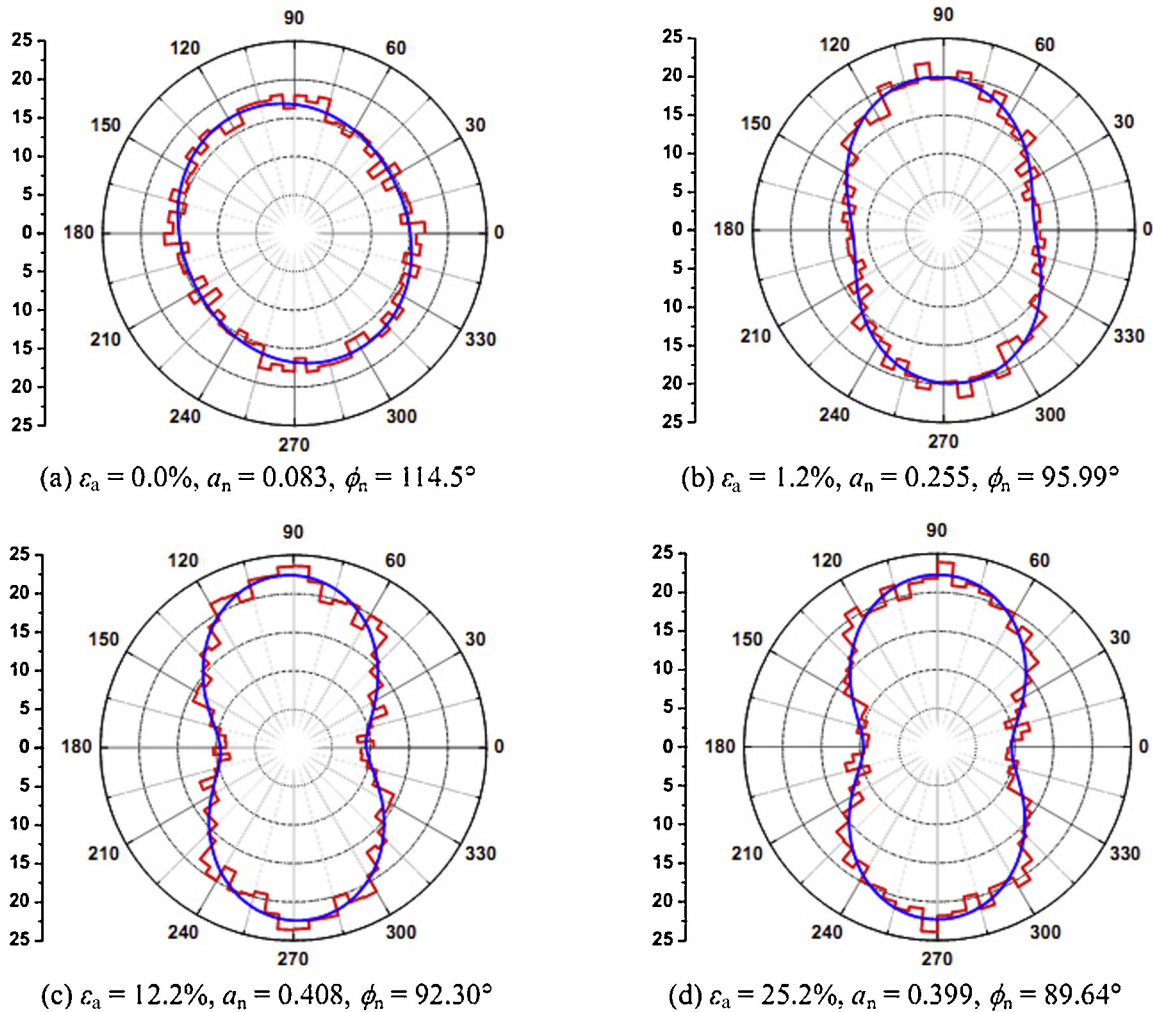(d) $\varepsilon_a = 25.2\%$, $a_n = 0.399$, $\phi_n = 89.64°$

Fig. 15. Angular distribution probability density (%) of the overall contact unit normal vector for specimen T-2.

unit normal vectors, where $\varepsilon_a = 25.2\%$, do not differ notably from those where $\varepsilon_a = 12.2\%$. Of particular interest is the observation in Fig. 11(b) that a_n of the S–L contact unit normal vector is close to that of the overall contact unit normal vector, which denotes an ensemble of the S–S, S–L, and L–L contact unit normal vectors. This observation is also supported by comparison of the rose diagrams in Fig. 13 with those in Fig. 15: the angular distribution of the S–L contact unit normal vector approximates that of the overall contact unit normal vector in the four shearing states.

As far as specimen T-1 is concerned, a_n of the L–L contact unit normal vector, similar to specimen T-2, exhibits an initial increase and then plateaus during shear (Fig. 11(a)). Meanwhile, a_n of the S–L contact unit normal vector experiences a monotonous increase prior to the onset of liquefaction, implying that the deviatoric shear loading causes S–L contacts to increasingly orientate into the loading direction and thus adapt to effectively carry the shear load. However, an interim decrease in a_n of the S–S contact unit normal vector occurs before it increases with subsequent shearing. This is because most S–S contacts are initially orientated perpendicular to the loading direction such that they are unable to sustain the external forces effectively and their orientations are expected to transit toward the loading direction upon the initial shearing. As revealed by the rose

diagrams in Fig. 16, the principal direction of anisotropy transits from ~0° (horizontal) at $\varepsilon_a = 0.0\%$, to ~90° (loading direction) at $\varepsilon_a = 1.2\%$. In other words, the initial shearing reduces the S–S contacts oriented horizontally and simultaneously increases the S–S contacts orientated in the loading direction. This adjustment in the S–S contact orientations leads to a temporary decrease of a_n.

Close scrutiny of Fig. 11 also reveals that the L–L contact unit normal vector generally has the strongest anisotropy, and the S–S contact unit normal vector has the weakest anisotropy. This suggests that large particles play a major role in sustaining the external forces whereby the external loads are principally carried by large particles through the microscopic force chains formed at the S–L and L–L contacts. Indeed, Fig. 17 indicates that the mean contact normal forces at the L–L contacts are the highest and the mean contact normal forces at the S–S contacts are the lowest. Fig. 18(a) and 18(b) also show that the main force chains in the reference area, shown by the dotted line, are mostly formed at the contacts between large particles (yellow).

Nevertheless, it should be mentioned that the substantial role of large particles in the formation of the main force chains does not exclude the role that the fine particles play in the force chains. As discussed previously, the evolution of the microstructures is highly dependent on the movement of fine particles in the soil skeleton
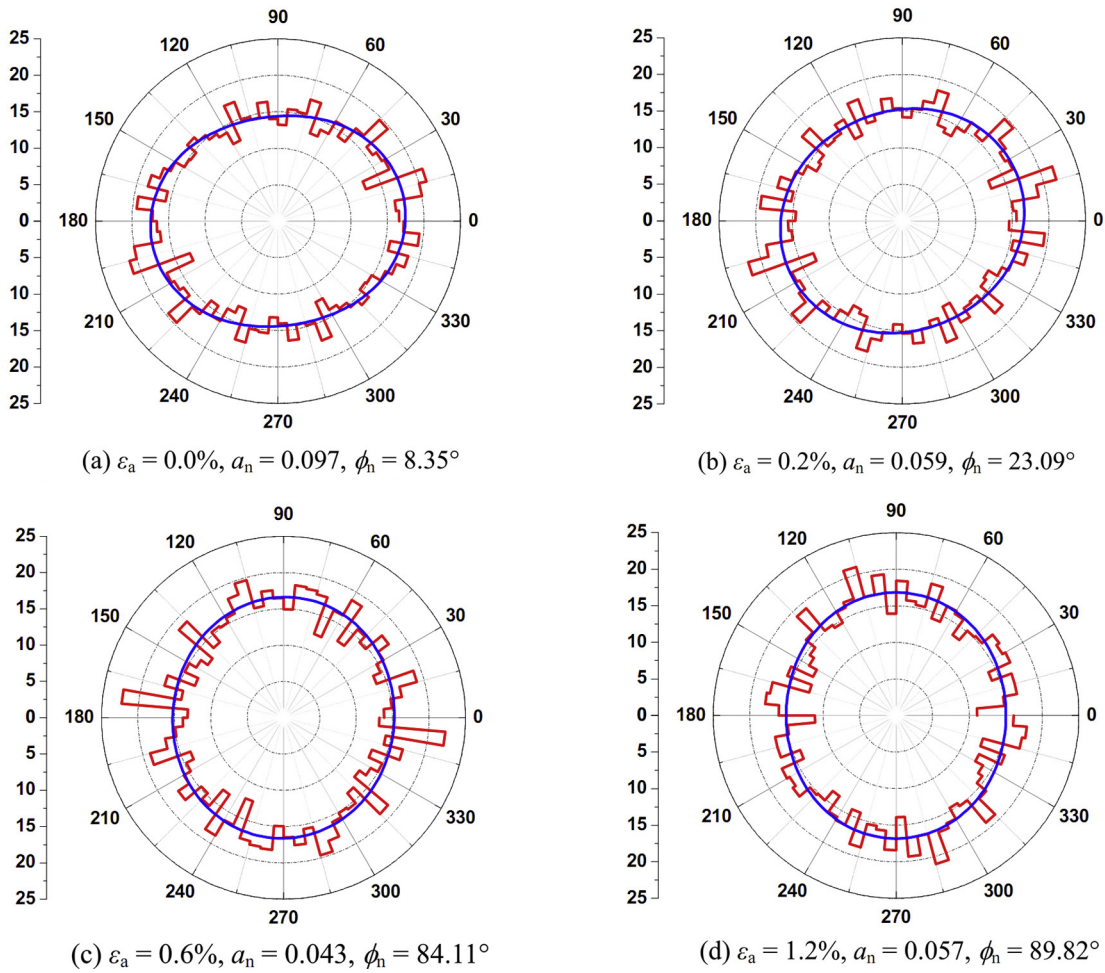
(a) $\varepsilon_a = 0.0\%$, $a_n = 0.097$, $\phi_n = 8.35°$ (b) $\varepsilon_a = 0.2\%$, $a_n = 0.059$, $\phi_n = 23.09°$

(c) $\varepsilon_a = 0.6\%$, $a_n = 0.043$, $\phi_n = 84.11°$ (d) $\varepsilon_a = 1.2\%$, $a_n = 0.057$, $\phi_n = 89.82°$

Fig. 16. Angular distribution probability density (%) of the S–S contact unit normal vector for specimen T-1.

and the role of large particles in carrying shear loads relies firmly on the supporting effect of fine particles.

Particle motion

The evolution of particle rotation and sliding ratios with increasing ε_a is shown in Figs. 19 and 20. The contacts at which the mobilized inter-particle friction coefficient (μ_s) is >0.9999 are regarded as sliding contacts. Fig. 19 shows that the rotation of both fine and large particles increases continuously during the entire shearing process. In particular, the degrees of rotation experienced by the fine particles are higher than the large particles, suggesting that fine particles rotate more freely. This is most likely because fine particles located at, or near, the contacts between large particles are prone to rolling, thus giving a more compressible soil skeleton. From Fig. 20 it can be observed that the S–L and L–L sliding ratios are higher than the S–S sliding ratios, suggesting that large particles are more inclined to slide.
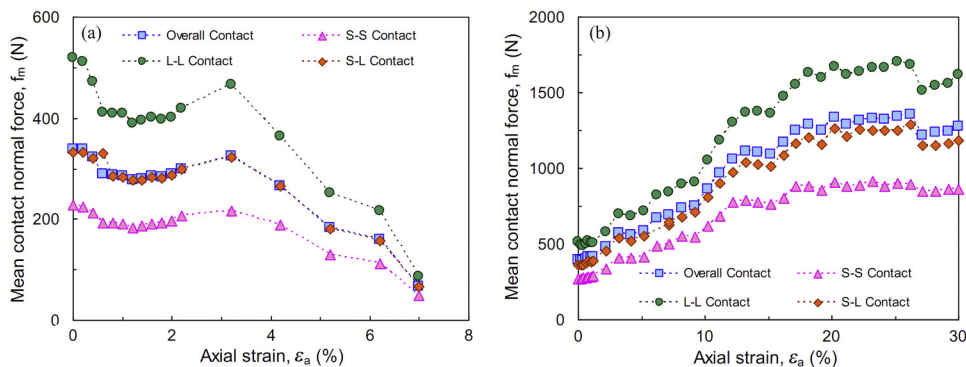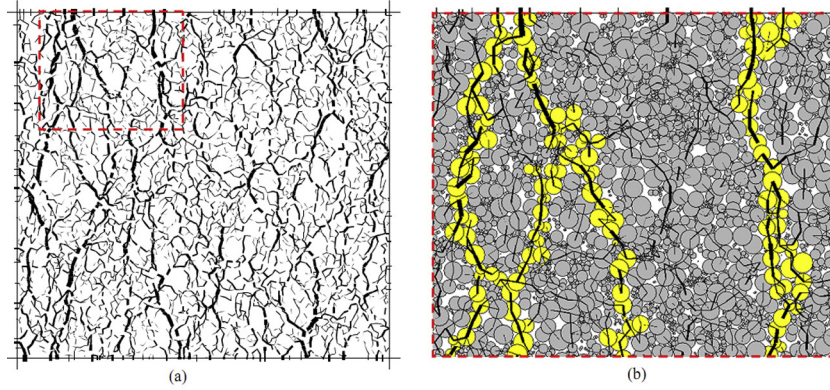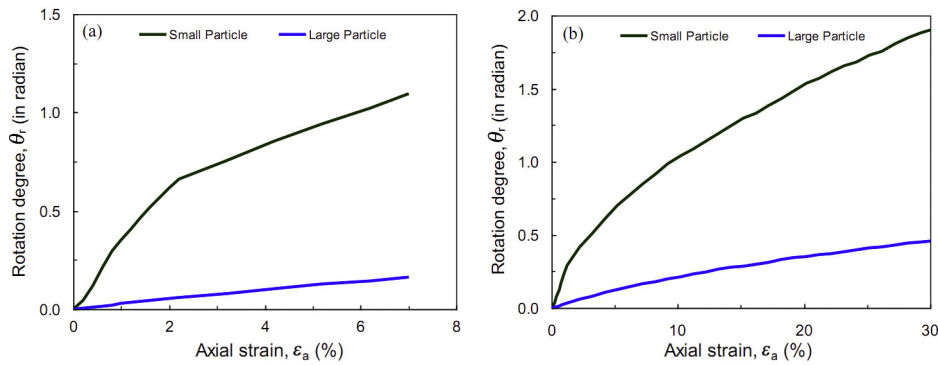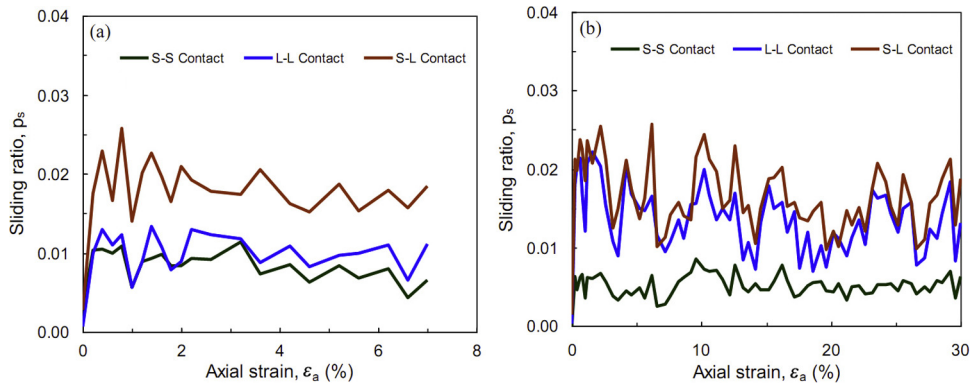

Fig. 17. Evolution of the mean contact normal forces with increasing axial strain for specimens: (a) T-1 and (b) T-2.

Fig. 18. Force chains at $\varepsilon_a = 4.2\%$ for specimen T-1: (a) a global view of the force chains in the specimen and (b) the main force chains in the reference area. (For interpretation of the references to color in the text, the reader is referred to the web version of the article.)

Fig. 19. Particle rotation in radian with increasing axial strain for specimens: (a) T-1 and (b) T-2.

Fig. 20. Sliding ratio of the various contact types for specimens: (a) T-1 and (b) T-2.

Conclusions

This paper presents a numerical investigation into the role of fine particles in the shear behavior of granular soil. The main findings are summarized as follows:

1. The simulation reveals that the participation of fine particles in the soil skeleton of granular soil increases the potential to contract and liquefy. The degree of contraction increases with increasing fines content. These findings are consistent with the previous work of Yamamuro and Lade (1997), Thevanayagam and Mohan (2000), and Yang and Wei (2012).
2. Fine particles play an important role in the evolution of the overall CN and soil structure while the large particles play a secondary

role. The liquefaction of granular soil with fine particles (silty sand) results mainly from the continuous loss of support from the S–S and S–L contacts that is caused by the removal of the fines from the soil skeleton. In the case of temporary liquefaction, fine particles initially move out of the soil skeleton at the initial shearing stage, rendering temporary contractive behavior and an interim decrease in the S–L and S–S CNs, followed by migration back into the soil skeleton upon further shearing. This contributes to the dilative shear response and rebound of the S–L and S–S CNs.
3. The S–S, S–L, and L–L contacts all tend to orientate into the loading direction during shear so as to effectively carry the external loads. The a_n of the S–S, S–L, and L–L contact unit normal vectors increase with shear strain until they reach a stable state. Under

conditions of complete liquefaction, a_n of the S–S contact unit normal vector may undergo an interim decrease because most S–S contacts are initially oriented horizontally and their orientations will undergo a transition toward the loading direction upon initial shearing. The external shear loads are primarily carried by large particles through the force chains formed at the S–L and L–L contacts.

4. Fine particles are found to be prone to rolling and rotating, whilst large particles are prone to sliding, mainly at the S–L and L–L contacts.

Acknowledgements

References

Been, K., & Jefferies, M. G. (1985). A state parameter for sands. *Géotechnique, 35*(2), 99–112.

Bobei, D. C., Lo, S. R., Wanatowski, D., Gnanendran, C. T., & Rahman, M. M. (2009). Modified state parameter for characterizing static liquefaction of sand with fines. *Canadian Geotechnical Journal, 46*, 281–295.

Chu, J., & Leong, W. K. (2002). Effect of fines on instability behaviour of loose sand. *Géotechnique, 52*(10), 751–755.

Cundall, P. A. (1971). A computer model for simulating progressive, large scale movements in blocky rock systems. In *Proceedings of the International Symposium on Rock Fracture, Vol. 2* Nancy, France, (pp. 129–136).

Dai, B. B. (2010). *Micromechanical investigation of the behavior of granular materials* (Doctoral dissertation). The University of Hong Kong, Hong Kong, China: Department of Civil Engineering.

Georgiannou, V. N., Burland, J. B., & Hight, H. W. (1990). The undrained behavior of clayey sands in triaxial compression and extension. *Géotechnique, 40*(3), 431–449.

Gu, X., Yang, J., & Huang, M. (2013). DEM simulation of the small strain stiffness of granular soils: Effect of stress ratio. *Granular Matter, 15*, 287–298.

Ishihara, K. (1993). Liquefaction and flow failure during earthquakes. *Géotechnique, 43*(3), 351–415.

Itasca. (2005). *User's manual for PFC2D*. Minneapolis, USA: Itasca Consulting Group, Inc.

Khalili, Y., & Mahboubi, A. (2014). Discrete simulation and micromechanical analysis of two-dimensional saturated granular media. *Particuology, 15*, 138–150.

Kuerbis, R. H., Negussey, D., & Vaid, Y. P. (1988). Effect of gradation and fines content on the undrained response of sand. In *Proceedings of the Hydraulic Fill Structures, No. 21* (pp. 330–345). ASCE, New York: Geotechnical Special Publication.

Lade, P. V., & Yamamuro, J. A. (1997). Effects of non-plastic fines on static liquefaction of sands. *Canadian Geotechnical Journal, 34*, 918–928.

Li, X. S., & Dafalias, Y. F. (2000). Dilatancy for cohesionless soils. *Géotechnique, 50*(4), 449–460.

Mahmud Sazzad, M. (2014). Micro-scale behavior of granular materials during cyclic loading. *Particuology, 16*, 132–141.

Mitchell, J. K. (1976). *Fundamentals of soil behaviors*. New York: Wiley.

Murthy, T. G., Loukidis, D., Carraro, J. A. H., Prezzi, M., & Salgado, R. (2007). Undrained monotonic response of clean and silty sands. *Géotechnique, 57*(3), 273–288.

Ni, Q., Tan, T. S., Dasari, G. R., & Hight, D. W. (2004). Contribution of fines to the compressive strength of mixed soils. *Géotechnique, 54*(9), 561–569.

Oda, M. (1982). Fabric tensor for discontinuous geological materials. *Soils and Foundations, 22*(4), 96–108.

Oda, M. (1999). Fabric tensors and its geometrical meaning. In M. Oda, & K. Iwashita (Eds.), *Introduction to mechanics of granular materials* (pp. 27–35). Rotterdam: A.A. Balkema.

Pitman, T. D., Robertson, P. K., & Sego, D. C. (1994). Influence of fines on the collapse of loose sands. *Canadian Geotechnical Journal, 31*, 728–739.

Rahman, M. M., Lo, S. R., & Gnanendran, C. T. (2008). On equivalent granular void ratio and steady state behavior of loose sand with fines. *Canadian Geotechnical Journal, 45*, 1439–1456.

Rothenburg, L., & Bathurst, R. J. (1989). Analytical study of induced anisotropy in idealized granular materials. *Géotechnique, 39*(4), 601–614.

Seed, H. B., & Harder, L. F., Jr. (1990). SPT-based analysis of cyclic pore pressure generation and undrained residual strength. In *Proceedings of the H. Bolton Seed Memorial Symposium, Vol. 2* Berkeley, USA, (pp. 351–376).

Thevanayagam, S., & Mohan, S. (2000). Intergranular state variables and stress-strain behaviour of silty sands. *Géotechnique, 50*(1), 1–23.

Thevanayagam, S., Shenthan, T., Mohan, S., & Liang, J. (2002). Undrained fragility of clean sands, silty sands and sandy silts. *Journal of Geotechnical and Geoenvironmental Engineering, 128*(10), 849–859.

Thornton, C. (2000). Numerical simulations of deviatoric shear deformation of granular media. *Géotechnique, 50*(1), 43–53.

Wood, D. M., Belkheir, K., & Liu, M. D. (1994). Strain-softening and state parameter for sand modeling. *Géotechnique, 44*(2), 335–339.

Yamamuro, J. A., & Lade, P. V. (1997). Static liquefaction of very loose sands. *Canadian Geotechnical Journal, 34*, 905–917.

Yang, J. (2002). Non-uniqueness of flow liquefaction line for loose sand. *Géotechnique, 52*(10), 757–760.

Yang, J., & Dai, B. B. (2011). Is the quasi-steady state a real behaviour? A micromechanical perspective. *Géotechnique, 61*(2), 175–183.

Yang, J., & Li, X. S. (2004). State-dependent strength of sands from the perspective of unified modeling. *Journal of Geotechnical and Geoenvironmental Engineering, 130*(2), 186–198.

Yang, J., & Wei, L. M. (2012). Collapse of loose sand with the addition of fines: The role of particle shape. *Géotechnique, 62*(12), 1111–1125.

Yang, S. L., Sandven, R., & Grande, L. (2006). Steady-state lines of sand–silt mixtures. *Canadian Geotechnical Journal, 43*, 1213–1219.

Zlatović, S., & Ishihara, K. (1997). Normalized behaviors of very loose non-plastic soils: Effects of fabric. *Soils and Foundations, 37*(4), 47–56.